Hydrothermal Ethanol Flames in Co-Flow Jets

M. C. Hicks[a], U. G. Hegde[b], J. J. Kojima[c]

[b]Corresponding author

Case Western Reserve University, Cleveland, Ohio, United States

Mailing address:

MS 110-3

NASA John H. Glenn Research Center

Cleveland, Ohio 44135

USA

e-mail: uday.g.hegde@nasa.gov

Tel: 1-216-433-8744

[a] NASA John H. Glenn Research Center, Cleveland, OH, United States

e-mail: michael.c.hicks@nasa.gov

[c] Ohio Aerospace Institute, Cleveland, OH, United States

e-mail: jun.j.kojima@nasa.gov

Abstract

Results on the autoignition and stabilization of ethanol hydrothermal flames in a Supercritical Water Oxidation (SCWO) reactor operating at constant pressure are reported. The flames are observed as luminous reaction zones occurring in supercritical water; i.e., water at conditions above its critical point (approximately 22 MPa and 374 °C). A co-flow injector is used to inject fuel (inner flow), comprising an aqueous solution ranging from 20 %-v to 50 %-v ethanol, and air (annular flow) into a reactor filled with supercritical water at approximately 24.3 MPa and 425 °C. Results show hydrothermal flames are autoignited and form diffusion flames which exhibit laminar and/or turbulent features depending upon flow conditions. Two orthogonal camera views are used; one providing a backlit shadowgraphic image of the co-flow jet and the other providing color images of the flame. In addition, spectroscopic measurements of flame emissions in the UV and visible spectrum are discussed.

Keywords: supercritical water oxidation; autoignition; hydrothermal flame; jet injection; high pressure

1. Introduction

Proper waste management for long duration space missions has remained a long standing technical challenge for NASA's mission planners due to the increased emphasis on resource reclamation and the cumulative volumes associated with any extended space exploration mission. Even short duration human space missions, such as the past missions of Skylab and Space Shuttle, and the current science missions carried out on the International Space Station (ISS), generate a considerable amount of waste. This waste is usually wet, voluminous, and biologically unstable with the major constituents comprising plastics (about 30% on average) and water (also approximately 30%) [1].

The water in the waste comes from a combination of food residues stuck to food pouches, hygiene wipes, and free liquids remaining in the drink pouches after consumption. It has been estimated that for a Lunar outpost each inhabitant generates between 6.8 kg to 9.6 kg of waste per day. Waste accumulation remains a significant problem and will require serious attention in the planning and design for the long duration space exploration missions currently envisioned; particularly with the Mars transit mission. In order to reduce the waste management system's "total equivalent mass" to minimize re-supply missions, it is essential to move toward closure of the environmental control and life support system [2]. This drive toward effective closure will be enabled by technologies that allow resource reclamation from the air, water, and waste streams. In addition, regenerative systems such as those designed to grow plants for food will require extensive resource reclamation (e.g., carbon dioxide, water and plant nutrients) from bio-waste streams in order to be practicable.

Supercritical Water Oxidation (SCWO) is a process where organic compounds can be efficiently oxidized in water above its critical point at approximately 374°C and 22 MPa. Under these conditions organic compounds and gases become completely soluble leading to extremely high reaction rates

between dissolved oxygen and organic materials [3, 4]. SCWO is often considered a “green” technology because of its ability to recover energy and reclaim water from wet waste streams without producing pollutants such as NO_x or SO_x, which require further scrubbing. The primary products of this oxidation mechanism are carbon dioxide and water, with the inorganic material precipitated out of solution as salt or converted into acids which can be neutralized in the effluent stream. SCWO is a promising technology [5] for processing solid entrained liquid waste streams since (i) pre-drying of waste is not required, (ii) product streams are benign, microbially inert, and easily reclaimed, (iii) organic waste conversion is complete and relatively fast, and (iv) with proper design and operation, reactions can be self-sustaining. In addition, because of the absence of inter-phase reactant transport due to the single phase nature of SCWO reactions, reaction timescales are greatly reduced and many of the complications associated with two-phase transport and processing in reduced gravity environments are eliminated which is an advantage for space missions.

Hydrothermal flames were first described by E.U. Franck who noted that flames could be generated in supercritical water because of the high miscibility of hydrocarbons (in this case methane) and oxygen in the medium [6]. As such, a “hydrothermal flame” is a classification of flames that occur in conditions when an environment is largely comprised of water at supercritical conditions. Hydrothermal flames have been studied in batch and semi-batch reactors [7].

Historically, supercritical water oxidation (SCWO) technologies have depended on maintaining conditions in the SCWO reactor where spontaneous ignition of localized hydrothermal flames was suppressed and the complete oxidation of hydrocarbon wastes occurs at relatively low temperatures. It was recognized that these flames, if not properly controlled in reactors for which these conditions were not designed, would lead to accelerated thermal wear on reactor components, would enhance

corrosion, and depending on the reactant stream, would result in increases in NO_x or other unwanted products [8].

Recently, however, a number of SCWO technologies and/or advanced reactor concepts have been proposed where controlled hydrothermal flames are used beneficially. This includes hydrothermal flames for thermal augmentation to initiate or sustain reactions or as a means of increasing conversion efficiencies for traditionally difficult waste streams, or for new applications, such as for hydrothermal spallation drilling [9-13].

Results reported in this study demonstrate the feasibility of spontaneously igniting and stabilizing hydrothermal flames in a SCWO reactor operating at constant pressure. Hydrothermal flames are observed as luminous reaction zones that occur when appropriate concentrations of fuel and oxidizer are present in supercritical water. A co-flow injector is used to inject fuel (inner flow), comprising an aqueous solution ranging from 20 %-v to 50 %-v ethanol, and air (annular flow) into a reactor filled with supercritical water at approximately 24.3 MPa and 425 °C. Two orthogonal camera views are used; one providing a backlit shadowgraphic image of the co-flow jet and the other providing color images of the flame geometry. In addition, spectroscopic measurements of flame emissions in the UV and visible spectrum are reported. The present work is an extension of the study presented in [14] on supercritical water jets to reacting jets and is complementary to experimental [15] and modeling [16, 17] work on flame autoignition.

2. Methods

2.1 SCWO Test Cell

The SCWO Test Cell (hereinafter “reactor”), shown in Fig. 1, is machined from Inconel 625 with a maximum design pressure of 34 MPa at 538 °C and is typically operated at conditions up to 25 MPa at temperatures up to 450 °C. The total enclosed test cell volume is 57 cm^3 and consists primarily of the

two orthogonal window bores 3.75 cm in diameter and 5.3 cm long. The end of each window bore is closed with a 4.13 cm diameter, 2.54 cm thick sapphire window with the C-axis perpendicular to the window face, which is polished and finished per NASA-HDBK- 6007 [18] specifications which assures consistency in window characteristics e.g, when they are replaced. These specifications include details for the rough removal, grinding, lap polishing, thermal annealing, and final buff polish of the windows.

Each window is sealed with a spin polished Ag plated Inconel C-seal. These seals are specialty items fabricated with a thin Au plating placed between the exposed Ag coating and a Ni strike coating applied directly to the Inconel surface. The purpose of the Au plating is to prevent leaching through the Ag coating of dissociated oxygen, which would ultimately react with the Ni strike coating. Without the impermeable layer of Au a layer of Ni0 was found to form resulting in blistering of the Ag pressure seal and an eventual leakage site. There is also a 3.75 cm diameter bore in the bottom of the reactor that is filled with a copper “plug” to reduce convective currents surrounding the co-flow injection assembly.

The reactor is heated by four electric cartridge heaters rated at 100 Watts each and located in four holes symmetrically placed around the center and in the body of the reactor. They are controlled with a Labview program using inputs from the thermocouples located in holes in the reactor’s body. There is also an electric heater located on each of the two inlet lines to pre-heat the test fluid to temperatures just above the bulk fluid temperature before entering the reactor. The injector, as shown in the inset of Fig.1 , shows the arrangement of the co-flow cross-sectional areas, having a ratio of 16:1 between the annular and core flow areas.

2.2 Diagnostics

Two cameras are used for imaging the injection hydrodynamics and the flame. The first camera (1024 × 1024 pixels, 30 fps equipped with a telecentric lens with an 0.11 cm depth of field), provides shadowgrapic imaging of the injection stream by using a collimated light source positioned at the

opposing window, as shown in Figure 2. This diagnostic is extremely sensitive to slight variations in temperature, particularly at near-critical conditions where density and refractive index dependence on temperature is very high, and can provide a high level of detail in the flow structure. The second camera (1392 × 1040 pixels) was used for color flame imaging and is placed orthogonal to the black and white camera on the left side of the reactor (not shown).

The window port opposite the color camera is blanked off with a 2.54 cm thick SS-304 disc through which four thermowells are inserted, each clocked at 90° and protruding to varying radial distances. The four thermowells each accommodate a thermistor (0.59 mm sheathed diameter) and are used for determining the local fluid temperature. However, because of the thin flame zone, the extremely steep temperature gradients, and the thermal inertia of the thermowells the thermistors are not suitable for providing flame temperatures [11] but do provide information on the bulk fluid temperatures in the cell. Note that for the autoignition tests described in Sections 3.1 and 3.2, the thermowells were moved away from the vicinity of the burner to avoid interference with the autoignition process. Otherwise, the lowest thermowell closest to the burner can serve as a hot surface and cause ignition as shown in Section 3.2. Optical emission spectroscopy was performed to measure spectral intensity in ultraviolet and visible regimes along the burner nozzle center axis at varying heights. Optical emissions were collected using a 105-mm, f/4.5 lens focused onto a single-core optical fiber (0.6 mm core diameter). The light was guided into an aberration-reduced imaging spectrometer (focal length 203 mm, stop set at f/3.88, slit width 20 micrometers and a grating of 300 grooves/mm) and was dispersed onto a back-illuminated imaging CCD camera with a 1340x400 pixel detector and a bit depth of 16 bit. Spectral signals were binned over a height of 14 pixels and typically accumulated on the CCD chip over 45 seconds to increase signal-to-noise ratio and all measurements were line-of-sight.

2.3 Experimental Procedures

For the tests reported in this work the fuel, comprising aqueous solutions of ethanol from 20%-v to 50%-v, was injected through the core and air was injected through the annulus. The reactor's bulk fluid, water, was heated to 425 °C and pressurized to 23.8 MPa at which point the core fuel flow was initiated at injection rates between 1ml/min to 2 ml/min, as measured at the high pressure piston pump. The transition to supercritical conditions of the water was evidenced by substantial buoyant convection in the bulk fluid, observed in the backlit images, even with small temperature differences (~ 1 °C). The strong buoyant convection commenced around 370 °C and subsided after the temperature exceeded 400 °C. This is the signature of the strong density variation with temperature during transition to the supercritical regime. Preheating of the fuel to near the bulk fluid temperature results in injection Reynolds number between 550 to 1100. Thus, the injected fuel stream was mostly laminar except near the tip region which would be unsteady [14]. Once the core flow was stabilized the annular flow (air) was initiated at an initial flow rate between 1.0 ml/min to 7.0 ml/min. Following ignition the core and annular flow rates were adjusted to the targeted steady state test conditions; these being a core fuel flow between 0.1 ml/min to 2.0 ml/min and a nominal annular air flow rate between 0.1 ml/min to 2.0 ml/min. It should be noted that the air flow was adjusted manually with a precision metering valve and it was difficult to precisely determine at low flow rates due to the limitations of the flow meter.

3. Results and Discussion

The autoignition process for injected fuel (ethanol-water blend) and oxidizer streams is discussed for laminar injection of the fuel. The fuel stream flow in this case is 50%-v ethanol at 2 ml/min which is approximately an injection Reynolds number of 1100 and an injection flow velocity of approximately 12 cm/s. Two co-flow air rates are considered i.e., 2 ml/min and 7 ml/min where the higher flow rate is conducive to enhancing turbulence behavior. Four different regimes concerning

autoignition have been identified in the literature for non-premixed flames [19]. These have been referred to as “no ignition”, “random spots”, “flashback”, and “lifted flame”. “No ignition” cases are not discussed in this paper, however, an “ignition map” for n-propanol has been provided earlier [15]. In the autoignition process described here, random spot regime preceded flame flashback (Section 3.2) and stabilization at the burner. Effects of fuel concentration and flow rates are then briefly discussed. Spectral emissions in the visible spectrum are provided for a blue appearing flame and for a flame which has yellow emissions as well.

3.1. Pre-autoignition behavior

The case with the lower air flow rate is considered first. A shadowgraphic image shortly after the air and fuel flows commence is shown in Fig. 3(a). The boundary between the fuel and air streams is visible and the fuel jet appears completely laminar. However, shortly thereafter on the time scale of ~ 1 s the shadowgraph begins to demonstrate significant changes in the flow field as in Fig. 3(b). The boundary between the central jet and the surrounding flow appears darker indicating strong density gradients and the downstream portion of the jet appears dynamically unstable similar to the breakpoint in a laminar jet. The first appearance of a flame appears in Fig. 3(c) in the furthest downstream portion of the image. It is evidenced by an expanded region with strong density gradients indicated by its relatively thicker dark boundary. This incipient flame then begins to propagate upstream. The flow upstream of the flame becomes more turbulent at this time as seen in Fig. 3(d). However, the flame extinguishes before propagating further upstream and leaves behind a considerably more turbulent flow field in the downstream regions of the jet as seen in Fig. 3(e). It is notable that the laminar portion of the jet exhibits more pronounced interface with the surroundings at this time.

The case with higher air flow rate exhibits similar features as shown in Fig. 4. The air stream is more turbulent in this case as seen in Fig. 4(a). The fuel jet becomes increasingly turbulent with time.

Figure 4(b) is taken 5.9 seconds later and the flow appears considerably more turbulent than in Fig. 4(a). The lower part of the flow closer to the burner also exhibits strong density gradients between the fuel and air streams. As in the case with the lower air flow, the first evidence of a flame appears in the downstream portion of the image. In Fig. 4(d) the flame has propagated slightly upstream. However, there is evidence of a burnout region between the jet and the flame. This is confirmed in the next image where the flame is absent and apparently extinguished.

It is interesting to consider the failure of these incipient flames to propagate to the burner. It is known that the leading edge of the flame on the upstream side (known as an edge flame) is associated with a burning (flame) velocity related to the rate at which reactants entering the flame are consumed. The flame velocity is related to the reaction rate, which is dependent on temperature and reactant concentrations, as well as species and thermal diffusivities [20]. The local turbulence scale and intensity level also impact the flame velocity. The flame can propagate upstream if the flame velocity exceeds the local flow velocity. On the other hand, the flame blows off if the flow velocity exceeds the flame velocity. However, the appearance of the burnout stage suggests added complications such as spatial and temporal variations in turbulence levels and reaction rates.

The incipient flame formation and burnout in conjunction with the increase in density gradients between the fuel and air streams in the upstream portions of the flow strongly suggest oxidation and heat release processes occurring even in the absence of a visible flame. The autoignition model for laminar flames [16] considered a similar situation where chemical reaction and heat release occur at the interface between the fuel and oxidizer. The local temperature increases and at some downstream location reaches the ignition temperature where the flame spontaneously ignites. The increase in turbulence in the experiment after both fuel and air injections are stabilized is likely due to the heat release enhancing density differences leading to significant buoyancy effects. These effects were not

considered in the model. The increased turbulence would enhance mixing between the fuel and air streams and presumably leads to an earlier (compared to the fully laminar case in the model) incipient flame formation. This finding has implications for the autoignition behavior in a microgravity environment of interest for NASA applications. Lack of buoyant mixing in microgravity could inhibit autoignition for laminar flows. Some degree of turbulence either by increasing injection velocities or by artificially inducing fluctuations could be required to ensure adequate mixing between the fuel and air streams leading to autoignition.

The local increases in temperature associated with the oxidation in the upstream part of the flow or in the incipient flame region have not been measured. Oxidation of ethanol under high pressures at the injection temperatures has been observed in earlier studies in both batch and flow reactors in which the fuel and oxidizer were premixed and at lower ethanol concentrations [21]. Chemical pathways were noted to be different compared to the high temperature case and involved the formation of peroxides and aldehydes.

It may be noted that incipient flame formation and extinction may occur more than once before a stable flame is finally established. In this respect, the incipient flames may be identified with the "random spot" generation observed in earlier studies [19]. As in that study the number of random spots prior to a successful autoignition may vary to some extent ; however, their statistics such as the mean number of random spots has not been investigated in the present work. In general, no more than 4 or 5 random spots prior to a successful autoignition have been observed in the tests conducted to date.

3.2. Flame autoignition and stabilization

Following a series of random spot generation and extinguishment, flame autoignition was found to occur during the tests described in Section 3.2. The autoignition and flame stabilization sequence for

the case with 2 ml/min air flow is shown in Fig. 5. It appears that over time with formation and extinction of incipient flames (“random spots”) the upstream flow becomes more turbulent. This may be seen by comparing Fig. 3(c) with the shadowgraph image of Fig. 5(a). It may be noted that Fig. 5 shows both the shadowgraph image as well as a corresponding color image which is close in time. The flame propagates upstream into the turbulent region in Fig. 5(b). As the flame propagates closer to the burner there is significant laminarization of the flow in the downstream regions. This may be due to the local increase in temperature which leads to an increase in the local viscosity [22]. Figure 5(d) shows the flame stabilized at the nozzle. Once the flame is stabilized at the burner, it becomes more yellow, indicating the presence of soot as shown in the next section, and the flame tip region becomes turbulent. Similar behavior is seen for the case with the higher air flow of 7 ml/min. The autoignition sequence of images for this case is shown in Fig. 6. The flow field is more turbulent than before and the propagating flame turns yellow prior to stabilization at the burner.

The flame propagation speed has been estimated from the images and is shown in Fig. 7 for both the low and high air flow rates. The average propagation speed is about 4.6 cm/s for the low air flow case (Fig. 5) and approximately 9 cm/sec for the higher air flow rate (Fig. 6). The propagation speed is not monotonic and reflects the changing conditions encountered by the edge flame in terms of both the flow as well as the local reaction rates. For example, for the higher flow rate case, the propagation speed reaches a minimum around x/d ~ 9, where x/d is the ratio of the distance from the burner exit plane, x, over the burner diameter, d. This location is close to where a local burnout seems to appear as in Fig. 6(b) (see also Fig. 4(d)). With this interpretation, the flame advance momentarily slows down due to lack of sufficient flammable reactants near the upstream flame edge. However, the reaction rate then increases with flowing fresh reactants and the flame propagation accelerates.

It is important not to have any hot surface in the vicinity of the flow which can serve as an ignition source. For example, in the presence of the thermowells, the ignition process is different. This is shown in Fig. 8 where ignition is seen to occur near the tip of the lowest thermowell. The case shown is for a 0.2 ml/min fuel flow rate of a 50%-v ethanol-water mix. There was no co-flow in this case but the bulk fluid in the cell was approximately a 40 % air-water mix. In these images, the frames from the two orthogonal cameras have been superimposed.

3.3. Flame spectroscopic emissions

Spectral measurements of flame emissions, although generally not quantitative, can provide useful insights into reactant mixing, reaction speciation, and reaction rates during combustion processes with a relatively simple diagnostic setup [23]. Flame spectral emission measurements are presented here for the two flames in Fig. 9(a) and 9(b) referred to, respectively, as Flame A and Flame B. Flame A shows a 30%-v ethanol flame with fuel flow of 1ml/min and a 2ml/min air flow at a bulk fluid temperature of 450 °C which exhibits yellow luminosity in the turbulent flame brush near the tip. Reducing both the fuel flow rate and the air flow rate results in near elimination of the sooty region as in Flame B which shows a 30%-v ethanol flame with fuel flow rate of 0.5 ml/min. The air flow rate was less than 1 ml/min, but not measured accurately, because of limitations of the precision metering valve associated with the air stream as noted in Section 2. 3

Emission spectra for Flame A in the wavelength range of 290 nm to 690 nm are shown in Fig. 10(a) for three heights above the burner exit plane, i.e., for x = 1 mm, 10 mm, and 20 mm. Consider first the spectrum at x = 1 mm which is at the base of the flame where it appears blue. Broadband emission is observed in the wavelength range of 350 to 540 nm and is generally attributed to CO_2^*, which may arise from a recombination of CO with an O atom or collisional excitation of a CO_2 molecule from its ground state [24]. It is likely that CH^* emission is masked by the CO_2^* emission. The line at

590 nm is due to sodium and is likely the result of contamination of the air stream. A weak OH* signal (around 310 nm) is observed as shown in the inset. At the locations x = 10 mm and x = 20 mm the spectrum is dominated by broadband emissions above 400 nm which is likely due to black body radiation from soot. This emission is much stronger at x = 20 mm which is in the yellow turbulent brush of the flame. Flame B is a blue non-sooty flame and its emission spectra is shown for a single height (x = 15 mm) in Fig. 10 (b). This location is in the blue turbulent brush region of the flame and the CO_2* emission bands are observed in the 350 nm to 540 nm wavelength range. There is no sodium line at 590 nm, which is consistent with the likelihood of it being a contaminant in the air line since the air flow rate is significantly lower for Flame B compared to Flame A. The emission spectra for Flame A, taken at the same height of 15 mm above the burner tip is also shown. Comparison of the two spectra highlight the observation that no OH* emissions or significant broadband emissions from soot are observed for Flame B. The general conclusion is that Flame B is much weaker in intensity compared to Flame A and, considering the apparent lack of OH* or soot, there may be significant differences in reaction pathway.

4. Conclusions

Results are reported from recent tests where hydrothermal flames autoignited in a Supercritical Water Oxidation (SCWO) Test Cell. A co-flow injector was used to inject fuel, comprising an aqueous solution of 20%-v to 50%-v ethanol and air into a reactor held at constant pressure and filled with supercritical water at approximately 24 MPa and 420 ℃. The flame pre-ignition, ignition, and stabilization processes are reported for a 50%-v fuel flow at 2 ml/min. The presence of chemical reactions and heat release are evidenced even close to the burner by changes in the shadowgraphic images. Incipient flame kernels are formed in the downstream regions of the flow. Autoignition and flame stabilization occur by the upstream propagation of the incipient flames to the burner. The flames appear to strengthen after stabilization on the burner. By adjusting the fuel and air flow rates varying degrees of flame luminosity

and sooting were observed. Spectral emission measurements of two different steady state flames were made over a spectral range spanning the ultraviolet (UV) to the near infrared (NIR). In non-sooting flame regions, the OH* signal at 310 nm is very weak or cannot be observed. Emission bands are observed in the wavelength range of 350 nm to 540 nm and attributed to CO_2*.

Acknowledgments

This work is funded under the Physical and Life Sciences Program managed by F. P. Chiaramonte at NASA Headquarters and managed locally by W. Foster and K. Bailey at NASA John H. Glenn Research Center. U. G. Hegde and J. J. Kojima were supported under NASA Contract NNC08BA08B. The authors would like to acknowledge the significant contributions of D. J. Gotti for his engineering support during the hardware design and assembly phase as well as his continued support during the conduct of these tests. The authors would also like to acknowledge the contributions of J. C. Owens for his engineering design of the imaging and data storage system.

References

[1] M. S. Anderson, M. K. Ewert, J. F. Keener, and S. A. Wagner. Life support baseline values and assumptions document. Technical Report NASA/TP-2015-218570, NASA JSC, 2015.

[2] R. Viskanta. Microgravity Research in Support of Technologies for the Human Exploration and Development of Space and Planetary Bodies. National Academy Press, Washington, DC, 2000.

[3] D.D. MacDonald, H. Arthur, R. Biswas, K. Eklund, N. Hara, G. Kakar, L. Kriksunov, C. Liu, S. Lvov, and J.Mankowski. Supercritical Water Oxidation Studies: Understanding the Chemistry and Electrochemistry of SCWO Systems. Final Progress Report of US Army Research Office DAAL 03-92-G-0397 and DAAH 01-93-G-0150, 1997.

[4] T.T. Bramlette, B. E. Mills, K. R. Hencken, M. E. Brynildson, S. C. Johnston, J. M. Hruby, H. C. Freemster, B. C. Odegard, and M. Modell. Destruction of DOE/DP Surrogate Wastes with Supercritical Water Oxidation Technology. Sandia Report SAND90-8229, 1990.

[5] S. A. Pisharody, J. W. Fisher and M.A. Abraham. Supercritical Water Oxidation of Solid Particulates. *Industrial Engineering and Chemistry Research*, 35, 4471-4478, 1996.

[6] E. U. Franck. Aqueous mixtures to supercritical temperatures and at high pressures. *Pure and Applied Chemistry*, 57(8), 1065-1070, 1985.

[7] C. Augustine and J. W. Tester. Hydrothermal Flames: From Phenomenological Experimental Demonstrations to Quantitative Understanding. *The Journal of Supercritical Fluids*, 47, 415-430, 2009.

[8] R. M. Serikawa, T. Usui, T. Nishimura, H. Sato, S. Hamada, and H. Sekino. Hydrothermal flames in supercritical water oxidation: investigation in a pilot scale continuous reactor. *Fuel*, 81 (9), 1147 -1159, 2002.

[9] M.D. Bermejo, P. Cabeza, J.P.S. Queiroz, C. Jiménez, and M.J. Cocero. Analysis of the scale up of a transpiring wall reactor with a hydrothermal flame as a heat source for the supercritical water oxidation. *The Journal of Supercritical Fluids*, 56, 21-32, 2011.

[10] P. Cabeza, J.P.S Queiroz, S. Arca, C. Jiménez, A. Gutiérrez, M.D. Bermejo, and M.J. Cocero. Sludge destruction by means of a hydrothermal flame: optimization of ammonia destruction conditions. *Chemical Engineering Journal*, 232, 1-9, 2013.

[11] P. Cabeza, M. D. Bermejo, C. Jiménez, and M. J. Cocero. Experimental study of the supercritical water oxidation of recalcitrant compounds under hydrothermal flames using tubular reactors. *Water Research*, 45(8), 2485-2495, 2011.

[12] J.P.S. Queiroz, M.D. Bermejo, F. Mato, and M.J. Cocero. Supercritical water oxidation with hydrothermal flame as internal heat source: Efficient and clean energy production from waste. *The Journal of Supercritical Fluids*, 96,103-113, 2015.

[13] T. Meier, D. Brkic, M. J. Schuler, M. Kant, and Ph. R. von Rohr. The potential of hydrothermal flames to induce spallation in gneiss. *Proceedings World Geothermal Congress*, 2015.

[14] U. Hegde, D. Gotti, and M. C. Hicks. The transition to turbulence of buoyant near-critical water jets. *The Journal of Supercritical Fluids*, 95,195-203, 2014.

[15] S. N. Reddy, S. Nanda, U. Hegde, M. C. Hicks, and J. A. Kozinski. Ignition of n-propanol-air hydrothermal flames during supercritical water oxidation. *Proceedings of the Combustion Institute*, 36, 2503-2511, 2017.

[16] P.V. Gordon, D. Gotti, U. Hegde, M. C. Hicks, M. J. Kulis, and G. I. Sivashinsky. An elementary model for autoignition of laminar jets. *Proceedings Royal Society*, A, 471-484, 2015.

[17] P. V. Gordon, U. Hegde, and M. C. Hicks. An elementary model for autoignition of free round turbulent jets. *SIAM Journal of Applied Mathematics*, 78, 2, 706-718, 2018.

[18] M.G. Ryschkewitsch. Handbook for recommended material removal processes for advanced ceramic test specimens and components. NASA-HDBK-6007, Nov-19-2007.

[19] S. K. Ghai and S. De. A Review on Autoignition in Laminar and Turbulent Nonpremixed Flames. *Combustion for Power Generation and Transportation*, A. K. Agrawal (ed.), 2017.

[20] K. K. Kuo. Principles of Combustion. John Wiley & Sons, Inc., New Jersey, 2nd edition, 2005.

[21] S. F. Rice and E. Croiset. Oxidation of Simple Alcohols in Supercritical Water III. Formation of Intermediates from Ethanol. *Industrial Engineering and Chemistry Research*, 40, 86-93, 2001.

[22] M. Ihme, and H. Pitsch. Effects of heat release on turbulent jet flows. Proceedings of the 5th International Conference on Turbulence and Shear Flow Phenomena, 991-996, Munich, Germany, 2007.

[23] A. G. Gaydon, The Spectroscopy of Flames, Chapman and Hall, London, 1957.

[24] H. N. Najim, P. H. Paul, C. J. Mueller, and P. S. Wyckoff. On the adequacy of certain experimental observables as measurements of flame burning rate. *Combustion and Flame*, 113, 312-332, 1998.

List of Figures

Fig. 5 Series of images showing formation of flame kernel, upstream flame propagation and stabilization of the diffusion flame for the 2 ml/min air co-flow case; where (a) reference time t = 0 s, (b) t = 0.166 s, (c) t = 0.300 s, (d) t = 0.400 s, and (e) t = 1.53 s.

Fig. 6 Series of images showing formation of flame kernel, upstream flame propagation and stabilization of the diffusion flame for the 7 ml/min air co-flow case; where (a) reference time t = 0 s, (b) t = 0.033 s, (c) t = 0.100 s, (d) t = 0.133 s, and (e) t = 0.166 s.

Fig. 7 Upstream flame propagation speed as a function of x/d, defined as the ratio of axial height above the burner's exit plane, x , to the diameter of the burner, d.

Fig. 8 Localized flame ignition near a thermowell.

Fig. 9 Images of 30%-v ethanol flame (a) Flame A with fuel flow of 1mL/min with 2ml/min air flow (b) Flame B with fuel flow of 0.5 ml/min and air flow less than 1ml/min.

Fig. 10 (a) Optical emission spectra from Flame A measured at various axial locations. The inset shows peak of OH* emission at x = 10 mm and (b) comparison of optical emission spectra from Flame A and Flame B measured at x = 15 mm.

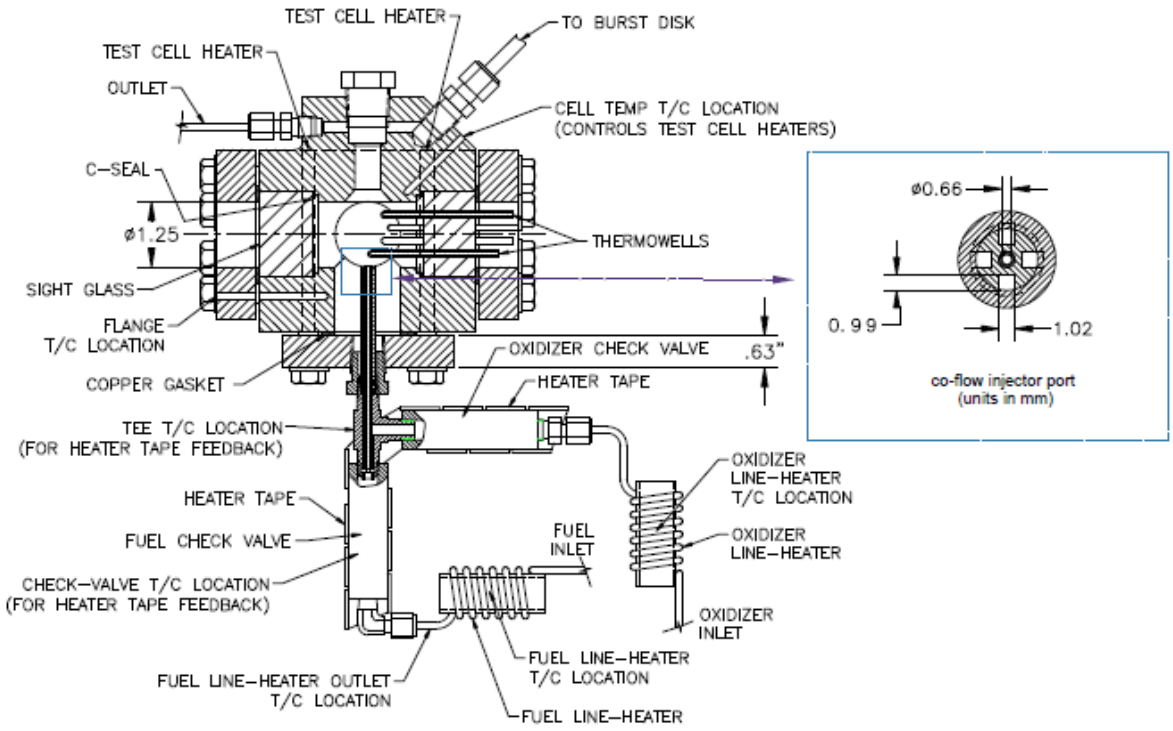
TEST CELL HEATER
TO BURST DISK
TEST CELL HEATER
OUTLET
CELL TEMP T/C LOCATION
(CONTROLS TEST CELL HEATERS)
C–SEAL
ø1.25
THERMOWELLS
SIGHT GLASS
FLANGE
T/C LOCATION
OXIDIZER CHECK VALVE
.63"
COPPER GASKET
HEATER TAPE
TEE T/C LOCATION
(FOR HEATER TAPE FEEDBACK)
OXIDIZER
LINE–HEATER
T/C LOCATION
HEATER TAPE
FUEL CHECK VALVE
FUEL
INLET
OXIDIZER
LINE–HEATER
CHECK–VALVE T/C LOCATION
(FOR HEATER TAPE FEEDBACK)
OXIDIZER
INLET
FUEL LINE–HEATER
T/C LOCATION
FUEL LINE–HEATER OUTLET
T/C LOCATION
FUEL LINE–HEATER
ø0.66
0.99
1.02
co-flow injector port
(units in mm)

Figure 1.

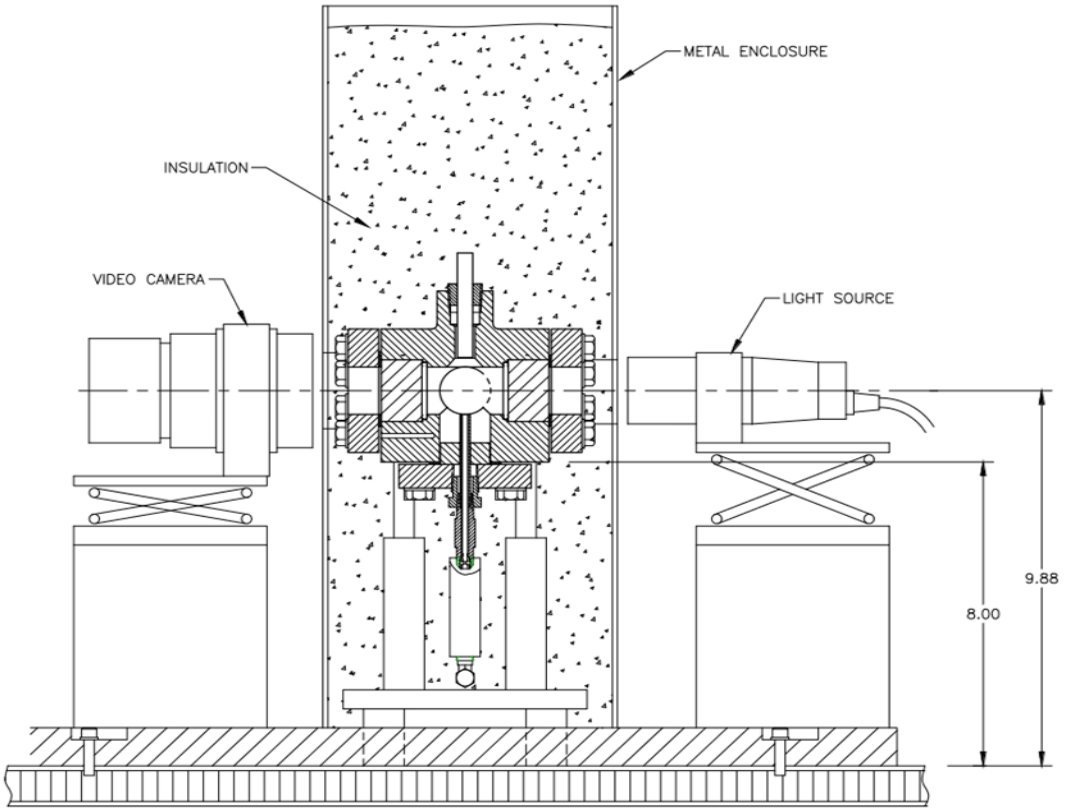
METAL ENCLOSURE
INSULATION
VIDEO CAMERA
LIGHT SOURCE
9.88
8.00

Figure 2.

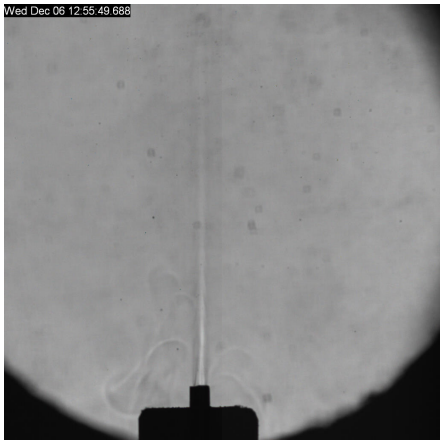

(a)

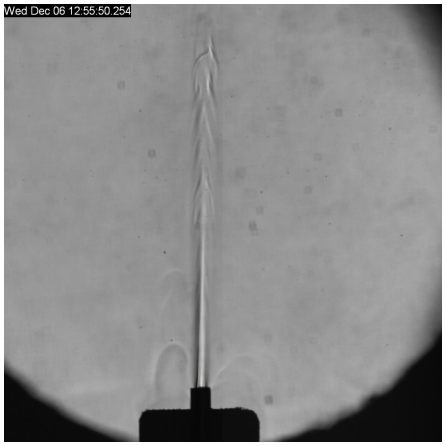

(b)

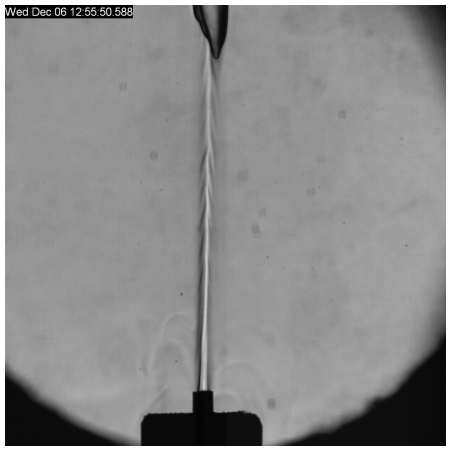

(c)

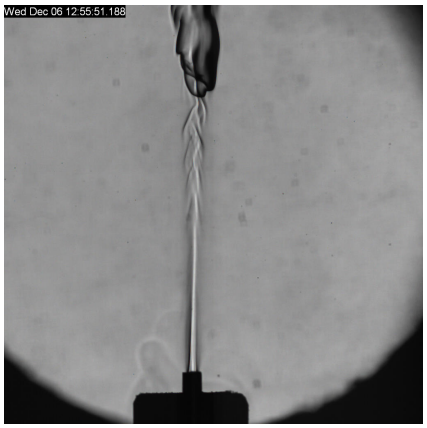

(d)

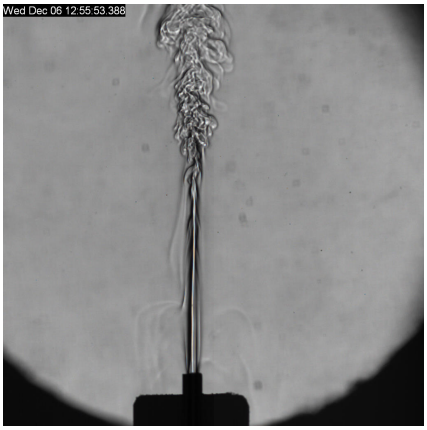

(e)

Figure 3.

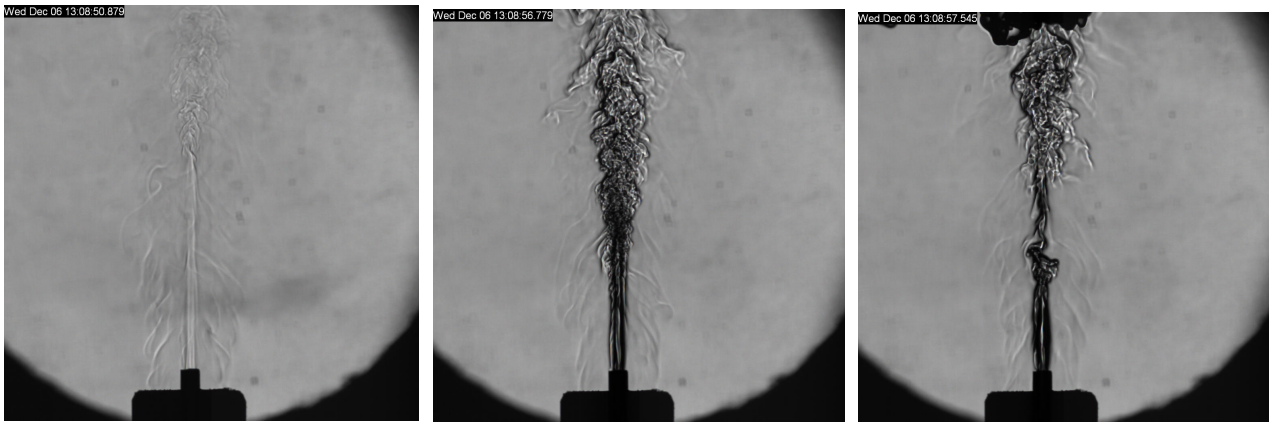

(a) (b) (c)

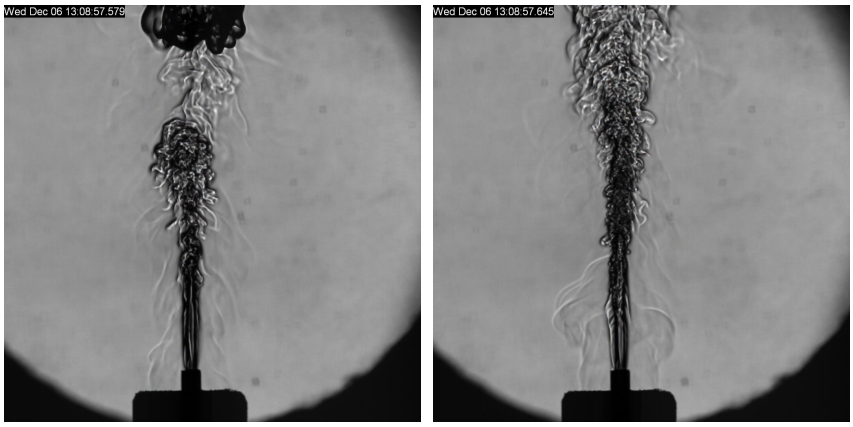

(d) (e)

Figure 4.

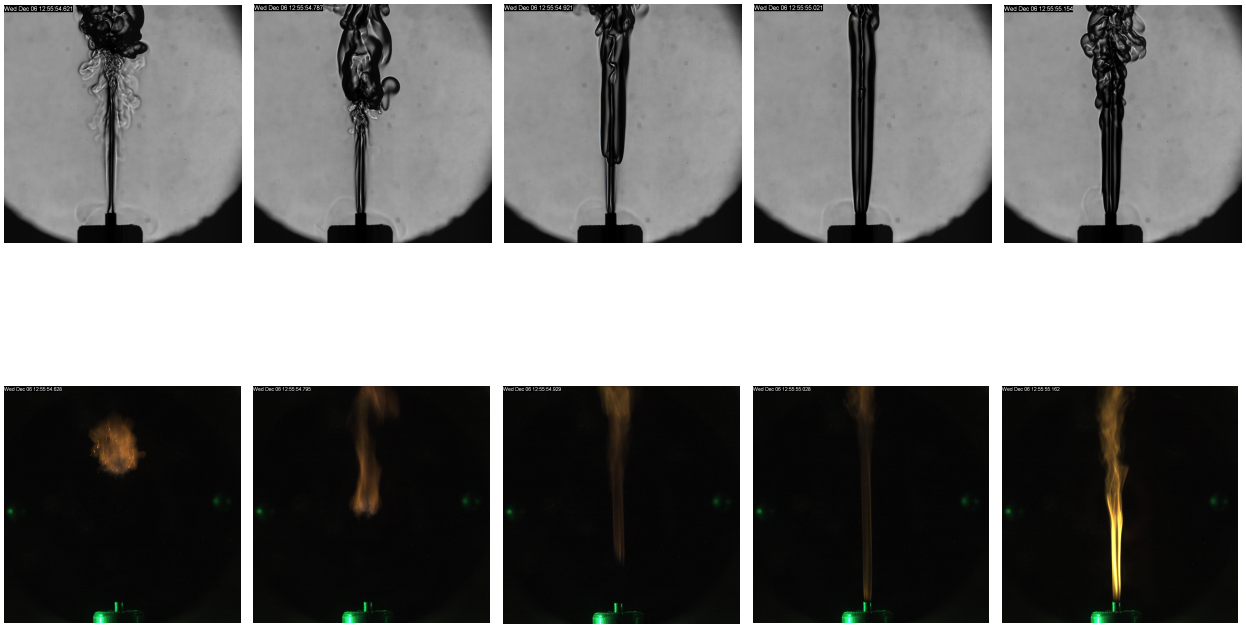

(a) (b) (c) (d) (e)

Fig. 5

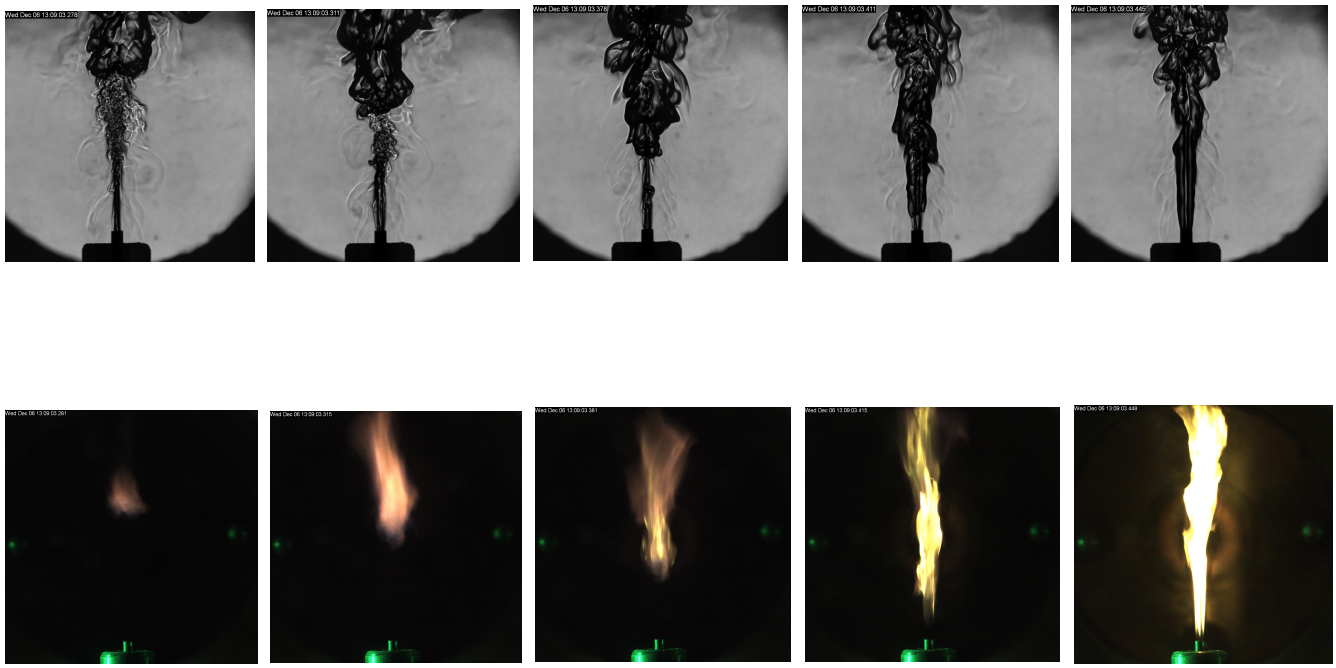

(a) (b) (c) (d) (e)

Figure 6.

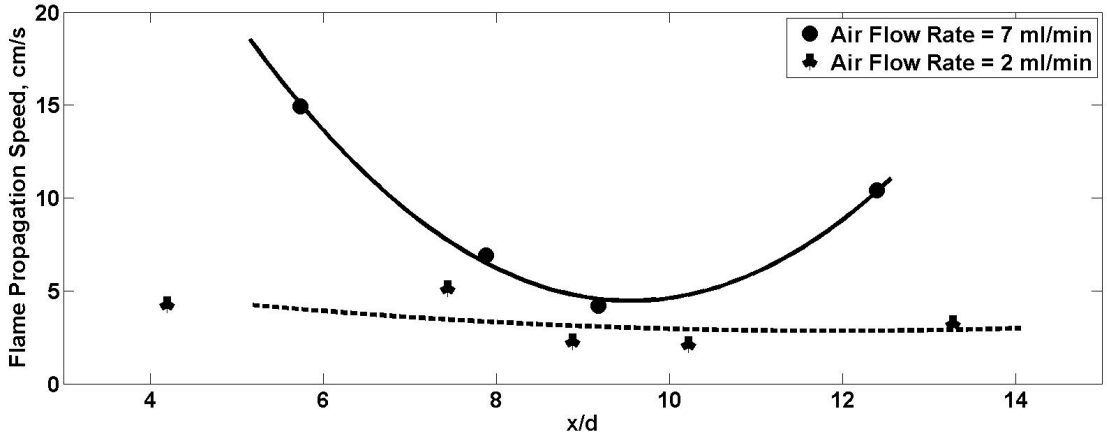
Air Flow Rate = 7 ml/min
Air Flow Rate = 2 ml/min
Flame Propagation Speed, cm/s
x/d
0
5
10
15
20
4
6
8
10
12
14

Fig. 7

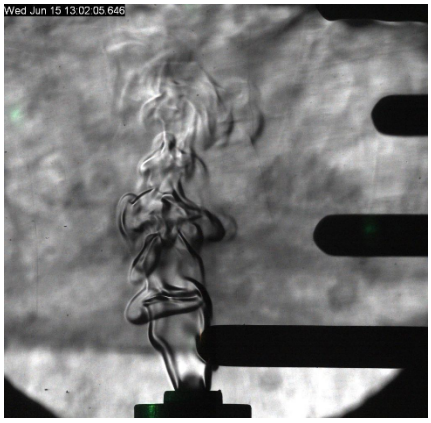

(a)

(b)

Fig. 8

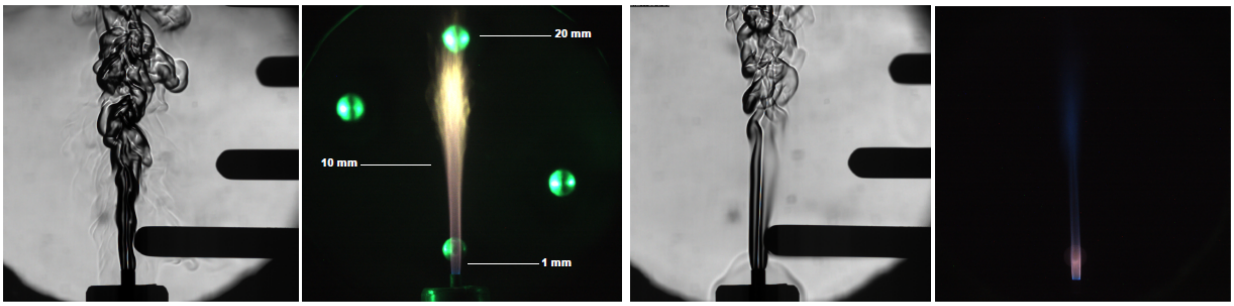

Figure 9

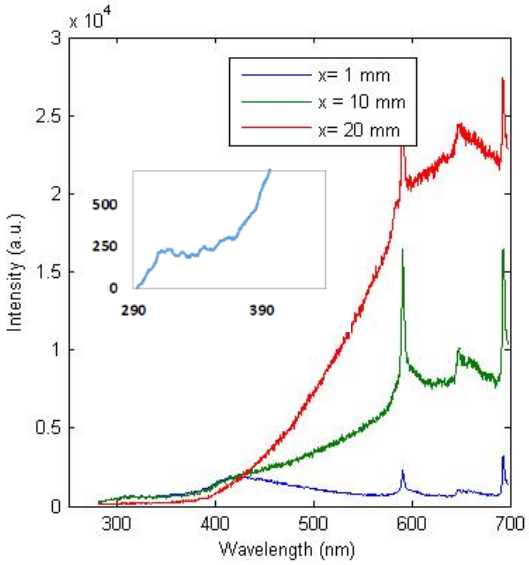
x 10^4
x= 1 mm
x = 10 mm
x= 20 mm
Intensity (a.u.)
Wavelength (nm)
500
250
0
290
390

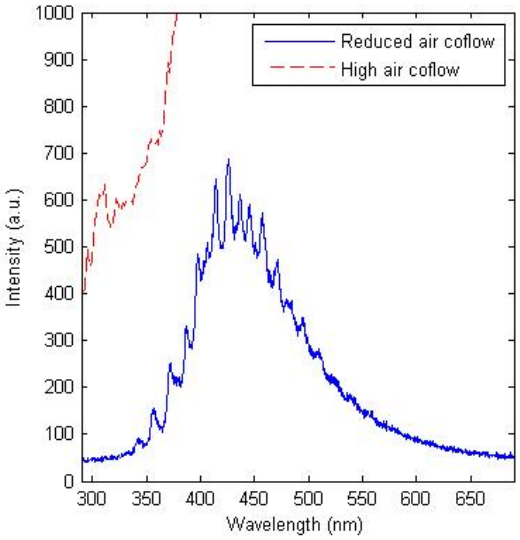
Reduced air coflow
High air coflow
Intensity (a.u.)
Wavelength (nm)

Figure 10